RESEARCH ARTICLE

INTERNATIONAL RESEARCH JOURNAL OF MULTIDISCIPLINARY TECHNOVATION

Asian Research Association

DOI: 10.54392/irjmt2416

# Enhanced Lung Nodule Segmentation using Dung Beetle Optimization based LNS-DualMAGNet Model

**K. Sathyamoorthy [a,*], S. Ravikumar [a]**

[a] Department of Computer Science and Engineering, Vel Tech Rangarajan Dr.Sagunthala R&D Institute of Science and Technology, Avadi, Chennai, India.

*Corresponding Author Email: sathyaveltechphd@gmail.com

DOI: https://doi.org/10.54392/irjmt2416

Received: 23-10-2023; Revised: 07-12-2023; Accepted: 16-01-2024; Published: 26-01-2024

**Abstract:** The study's focus is on lung nodules, which are frequently connected to lung cancer, the world's most common cause of cancer-related deaths. In clinical practice, a timely and precise diagnosis of these nodules is essential, albeit difficult. For diagnosis, the study used CT scans from the Lung Image Database Consortium and the LIDC-IDRI dataset. Noise reduction with a Gaussian Smoothing (GS) Filter and contrast enhancement were part of the preprocessing. With a Dual-path Multi-scale Attention Fusion Module (DualMAF) and a Multi-scale Normalized Channel Attention Module (MNCA), the study presented the LNS-DualMAGNet model for lung nodule segmentation. These modules improve interdependence across channels and semantic understanding by utilizing novel approaches such as Depthwise Separable Convolutions and attention mechanisms. For increased performance, the model also incorporates DSConv and a Resnet34 block. The Dung Beetle Optimization Algorithm (DBOA) was used for tuning the hyperparameter of the proposed classifier. Findings indicated that the proposed model performed better than the existing approaches, attaining a 0.99 accuracy and DSC, indicating its potential to enhance lung nodule segmentation for clinical diagnosis.

**Keywords:** Computed Tomography, Convolutional Neural Network, Gaussian Smoothing Filter, Contrast Enhancement, Dung Beetle Optimization Algorithm

## 1. Introduction

Lung cancer is one of the primary causes of cancer-related deaths globally [1]. Lung cancer diagnosis made by hand is subject to intra- and inter-reader variance. Lung cancer's most significant symptom is pulmonary nodules [2]. Lung segmentation is a critical step in the nodule identification procedure. Precise segmentation of the lung structures is essential for an automated computerised aided detection (CAD) system for lung cancer since it minimises the search space and enhances the diagnosis of lung nodules. However, the homogeneities that occur in lung structures-that is, the lungs have similar intensities with the neighbouring lung structures-present difficulties for lung segmentation. Annotated lesions on marked-up diagnostic lung cancer scans are included in the LIDC-IDRI collection [3]. It is for the improvement and evaluation of lung cancer detection and diagnosis.

Finding lung nodules is essential for both diagnosis and identification of lung cancer. Reducing the search space can help make the difficult work of lung nodule detection less complicated. To do this, the lung lobes are segmented prior to candidate nodule detection [4, 5].

Lung nodule appearances differ substantially. Although nodules are normally spherical in shape, they can become quite complex when they are connected to or encircled by other anatomical structures. There is a correlation between the type of lung nodules and their malignancy. The risk of lung cancer is higher in intra-parenchymal and optical ground glass (GGO) type nodules than in those that are confined to the surrounding structures alone. The intensity distribution and relative positions of nodules determine their type [6]. They are also classifiable:The terms "circumscribed" (W), "vascularized" (V), "juxta-pleural" (J), "pleural-tail" (P), "pleural surface" (J), "pleuralized" (V), "situated in the very centre of the lung and not connected to any other tissues," and "GGO" (G) refer to the various anatomical regions of the lung related to blood vessels [7], which is identical to W but differs in that it has a nonsolid CT value distribution. Computer Tomography (CT) is the gold standard for diagnosis in clinical practise since it can obtain fine-grained data for lung lesions and surrounding structures [8, 9].

CNNs, or convolutional neural networks [10, 11] are a powerful tool for lung nodule diagnosis because they can automatically segment images from medical situations. These networks excel in recognising intricate

patterns and textures in lung images, which facilitates more precise identification of potential nodules. CNNs analyse big datasets to process visual data efficiently [12]. This significantly reduces false positives and negatives, enabling radiologists to identify patients with greater accuracy. Due to their adaptability, efforts are still being made to enhance CNN architectures to enable them to manage a diverse array of nodule kinds, sizes, and complexity. Early detection programmes could be revolutionised by CNN integration with computer-aided diagnostic systems, which would also give medical practitioners reliable diagnostic tools quickly and accurately [13].

### 1.1. Main Contributions

❖ Employed Techniques for Image Enhancement:

For more precise diagnosis, CT image preprocessing from the LIDC-IDRI and Lung Image Database Consortium uses contrast enhancement method along with GS filter.

❖ Innovative Segmentation Model:

LNS-DualMAGNet model for is proposed lung nodule segmentation. Important elements include:

- **Inclusion of DualMAF:** Improves the understanding of the network by creating semantic connections between high- and low-level channels.
- **MNCA module:** Enhances segmentation accuracy by reinforcing channel interdependence through the use of DSConv, atrous convolution, and channel attention mechanism.
- **Enhanced Encoder-Decoder Backbone:** Using DSConv and pretrained Resnet34 blocks together to improve network performance even more.

❖ Application of DBOA:

Adoption of the sophisticated swarm intelligence method known as DBOA for LNS-DualMAGNet model hyperparameter tuning.

### 1.2. Organization of the work

The format of the paper is as follows: On the other hand, Section 2 analyses pertinent material in much more detail. Section 3 provides a brief summary of the suggested paradigm, while Section 4 reports the study's findings and provides a description of the validation process. Section 5 provides a final overview of the findings, capping up the effort.

## 2. Related works

The results of region growth, Otsu, and DC-U-Net of segmented lung CT were compared with Chen K-b *et al*.'s Dilated convolution merged with a proposed U-Net network [14]. The performance of each algorithm was evaluated using the Dice coefficient, Precision, Recall, and Intersection over Union (IOU) metrics. The segmented picture of DC-U-Net was found to be more accurate than the segmented images of the widely used segmentation algorithms, Otsu and region growth. DC-U-Net produced a Dice coefficient of 0.9743 and an IOU of 0.9627, which were both much higher and close to 1 in contrast to the other two algorithms.

Selvadass, S. *et al.* [15] revealed how to generate an atrous convolution augmented U-Net by concatenating each encoder and decoder route step is followed by dilated convolution blocks. This technique helped to extract important components from the feature maps and led to the model's perfect convergence. The publically available LIDC-IDRI dataset was mostly used in the evaluation. The average Dice Similarity Coefficient (DSC) was 81.10%, and the Intersection over Union (IoU/Jaccard Index) was 72.24%, according to the findings. The exploratory analysis's findings demonstrated that the architecture worked better.

Agnes, S. A. presented pyramid-dilated dense U-Net (PDD-U-Net), a novel deep learning-based segmentation model, to clearly distinguish lung regions from the entire CT scan [16]. This approach efficiently gathers and maintains multi-resolution spatial data by integrating pyramid-dilated convolution blocks. To improve the segmented output, shallow or deeper stream properties were introduced to the nested U-Net architecture at the decoder side. The suggested PDD-U-Net model outperformed earlier segmentation techniques when evaluated on lung CT datasets. It found that the dice coefficients for the LIDC-IDRI database were 0.983 and the LCTSC dataset was 0.994.

Modak, S. *et al.* demonstrated a new technique for segmenting nodules using graph clustering [17]. The image was pre-processed in order to identify the region of interest and extract lung parenchyma. Super-pixels and patch-breaking were achieved by patch-wise iterative graph clustering; hierarchical clustering was then used to combine the superpixels into different architectures. The proposed method showed good segmentation performance with 89.32% is a high average sensitivity, 0.88 is the average dice score, and 0.81 is the intersection over union score. It fared better than a number of cutting-edge techniques applied in the field.

Agnes, S. A., [18] proposed Wavelet U-Net++ is a novel approach for precisely segmenting lung nodules. By employing wavelet pooling in combination with the U-Net++ architecture to extract This method improved the accuracy of segmentation by extracting high- and low-frequency data from the image. Given that the average IoU is 0.878 and the average dice coefficient is 0.936, the experimental findings on the LIDC-IDRI dataset demonstrated higher performance in contrast to the

most sophisticated segmentation approaches. The network was able to identify irregular and tiny nodules better when wavelet pooled with Tversky and CE loss was combined.

Cai, Y *et al.* [19] suggested a 2D Multi-level Dynamic Fusion Network (MDFN) to improve the restoration of complicated edges by providing accurate segmentation of lung nodules and detailed edge data. This network employed a deep feature fusion decoder, a self-calibrated encoder, and a multi-scale spatial and channel feature selection module (MSCFS). With a median DSC of 89.19% and Hausdorff distance of 2.353 mm, MDFN outperformed other sophisticated methods in trials conducted on the publicly available dataset LUNA16.

The LUNA-16 dataset was utilised in the development and evaluation of a deep learning system (DB-NET) for pulmonary nodule recognition by Bhattacharyya, D., *et al* [20]. In comparison to the present U-NET model, the resource-efficient design known as DB-NET earned a dice coefficient index of 88.89%. With the help of mask class weights and the Mish nonlinearity function, it demonstrated accuracy that was on par with that of human specialists in segmentation.

Usman, M. *et al*. developed a technique for dividing lung nodules into two stages [21]. Originally, the lung nodules in the axial slice of thoracic CT scans was segmented using a dual-encoder-based hard attention networks (DEHA-Net). ROI masks for neighbouring slices were automatically created by the adaptive area of interest (A-ROI) approach. The lung nodule was then inspected from the coronal and sagittal views with DEHA-Net. The suggested method shown a notable enhancement and resilience to varying types, dimensions, and configurations of lung nodules when evaluated using the LIDC/IDRI dataset. It obtained a sensitivity of 90.84%, an average dice score of 89.56%, and a positive predictive value of 87.91%, respectively.

The Hybridized Faster R-CNN (HFRCNN) was employed in Srivastava, D., *et al*.'s study [22] to detect lung cancer early on. Rapid R-CNN has been used for a number of purposes, such as identifying important objects in medical images such as CT and MRI scans. In an effort to support the early detection of lung cancer, a number of research studies have examined various methods for identifying lung nodules in scanned images that may be indicators of the disease. One such model was the two-stage, region-based entity detector known as HFRCNN. It started by producing a set of suggested regions, which it then used a convolutional neural network (CNN) to classify and refine. A unique dataset was employed during the model's training phase, producing significant results. The proposed model outperformed a number of previously published techniques, achieving a detection accuracy of over 97%.

A context feature fusion and attention mechanism-based network called CFANet was presented in the paper by Cao, R., *et al.* [23] for small target segmentation in medical images. In order to improve segmentation performance, CFANet combined two essential modules, effective channel spatial attention (ECSA) and context feature fusion (CFF), which were based on the U-Net architecture and consisted of an encoder and a decoder. Contextual data from various scales was used by the CFF module to enhance the depiction of small targets. The network had successfully gathered both local and global contextual cues that are essential for precise segmentation by combining multi-scale features. By integrating attention mechanisms at the spatial and channel levels, the ECSA module further enhanced the network's capacity to detect long-range dependencies by enabling the network to concentrate on information-rich regions while suppressing irrelevant or noisy features. LUNA16, WORD, Thoracic OAR, and ADAM are four difficult medical image datasets on which extensive experiments have been conducted. According to the experimental findings, CFANet performed better in terms of segmentation accuracy and robustness than the most advanced techniques. The suggested technique showed great promise in a range of clinical applications by effectively segmenting small targets in medical images.

In the paper [24], Lyu, Y., & Tian, X. presented a novel technique for lung field and heart segmentation called MWG-UNet (multiple tasking Wasserstein generative adversarial network U-shape network). This approach leverages the attention mechanism to improve the generator's segmentation accuracy and overall performance. In particular, the suggested method outperformed sub-optimal models in terms of specificity by 0.28%, 0.90%, 0.24%, and 0.90%, and outperformed other models in terms of Dice similarity, precision, and F1 score, reaching 95.28%, 96.41%, and 95.90%, respectively. Still, the IoU value had fallen short by 0.69% compared to the best model. The outcomes demonstrated the suggested method's significant ability to segment the lung fields. Dice similarity and IoU values of 71.16% and 74.56% were attained in the multi-organ segmentation results for the heart, while 85.18% and 81.36% were attained in the segmentation results for the lung fields.

### 2.1. Research gap

Upon reviewing the context of research on lung nodule segmentation and diagnosis, numerous developments and methods have been put forth by different scientists. But in spite of these worthwhile additions, every strategy has some shortcomings and restrictions. High accuracy was attained when Chen K-b et al. combined U-Net network with Dilated convolution, but the potential of semantic interdependence was not fully utilized and there was insufficient investigation of multi-scale attention mechanisms. The atrous

convolution augmented U-Net by Selvadass, S. et al. showed encouraging results, but there is still room for improvement in convergence and precision as evidenced by the average Dice Similarity Coefficient (DSC) and Intersection over Union (IoU/Jaccard Index) not reaching optimal segmentation accuracy. Agnes, S. A.'s pyramid-dilated dense U-Net showed improved segmentation performance; however, the model's performance could still use some fine tuning to capture fine details in lung regions, particularly in more complicated datasets. The graph clustering method by Modak, S. et al. performed well in segmentation, but it struggled to handle irregularly shaped nodules and extract finer details from the image, which reduced overall accuracy. Wavelet U-Net++ by Agnes, S. A. demonstrated potential in identifying irregular nodules, but it may encounter difficulties managing minuscule nodules and attaining consistently good performance on a variety of datasets. The 2D Multi-level Dynamic Fusion Network (MDFN) by Cai, Y et al. demonstrated advances in detailed segmentation and edge restoration, but there was room for improvement in handling complex edges and fine-tuning nodule boundaries. While DB-NET by Bhattacharyya, D., et al. showed promise, more research may be needed to handle edge cases and increase segmentation precision. Usman, M. et al.'s two-phase segmentation method demonstrated significant progress in handling different nodule shapes; nevertheless, more work is required to guarantee stability in the face of different nodule sizes and kinds. The method described in this paper offers a novel LNS-DualMAGNet model in order to overcome these drawbacks. It incorporates several cutting-edge elements, such as the MNCA and DualMAF, and it makes use of the DBOA for hyperparameter tuning. Due to its comprehensive architecture, the model not only achieves better performance metrics (0.99 accuracy and DSC) than the previously mentioned methods, but it also overcomes the limitations of existing methodologies in capturing semantic interdependence and multi-scale attention. This indicates that it has the potential to greatly improve lung nodule segmentation accuracy and clinical diagnosis, going beyond the constraints noted in the context of existing research.

## 3. Proposed Methodology

The actions required to put into practise the recommended method are shown in the schematic in Figure 1. This section covers the following procedures: image preprocessing using GSFilter and contrast enhancement, lung nodule class segmentation using LNS-DualMAGNet, and hyperparameter tuning using DBOA.

### 3.1. Dataset Description

The LIDC-IDRI dataset [25] was used in this investigation, which comprised 1018 clinical cases of thoracic CT scans. These scans were from different facilities, therefore the image quality differed. Slices of 512 x 512 pixels with thicknesses ranging from 1 to 5 mm and pixel spacings between 0.6 and 0.8 mm comprised each scan. For every CT scan, eight annotations were independently created by four seasoned thoracic radiologists. A consensus diagnosis was obtained by collaborative evaluation, and reliability was guaranteed by incorporating nodules identified in two or more annotations to minimise errors due to human annotation. Five unique categories were identified by the radiologists and applied to 1738 nodules: W (905, 52.0%), P (329, 19%), V (219, 12.5%), G (82, 6%), and J (203, 11.5%). The initial CT scans had 512 × 512 pixels, having an in-plane spacing of 0.4 to 1.0 mm and slice thicknesses of 0.5 to 3 mm. To maintain a 1 mm in-plane spacing and center the nodules at their gravity center, volumes were resampled to 64 × 64 × 64 $mm^3$.

During the model-building procedure, 20% of each type of nodule was set aside for testing and the remaining 80% was randomly assigned for training and validation. Creating and validating a robust classification model especially for nodules in a subset of the LIDC-IDRI dataset was the aim of this effort. The primary objective was to increase the accuracy of nodule characterization, which offers nodule diagnostics intriguing prospects for advancement.

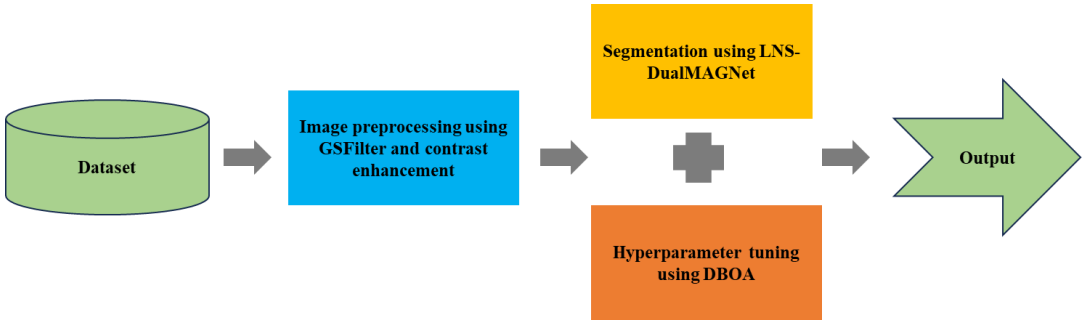


**Figure 1.** Workflow of the proposed model

## 3.2. Preprocessing of Images

### 3.2.1. Image Noise Removal Technique using GSFilter

CT scans imaging methods can produce lung nodule images that contain Gaussian noise. However, as part of the preprocessing procedures, this study used a GS Filter. By applying a Gaussian function to blur or smooth the image, this filter is frequently used to reduce noise in images. This may help to mitigate the presence of Gaussian noise that may have initially been present in the lung nodule images. Consequently, even though Gaussian noise may be present in raw images, this GSFilter probably tried to reduce its influence on the analysis and lung nodule segmentation that followed.

#### 3.2.1.1. GSFilter

To lessen Gauss noise at specific spots in the lung nodule image, a specialised filter called the GSFilter is applied. Poisson is created, however, by the statistical properties of electromagnetic waves, such as gamma or X-rays forms a convolution matrix using values from the Gaussian distribution to depict the approximate Gaussian distribution (or "bell-shaped" hump) using a convolutional kernel [26]. We can stop the kernel at three standard deviations from the average since, in reality, the distribution of values is effectively zero at this point. In principle, the distribution is non-zero everywhere, necessitating an infinitely long convolution kernel. Since the distribution of noise amplitude is regular, the median value is zero. Thus, in order to blur the image or eliminate noise in the two dimensions given in (1), the Gaussian filter generates this kernel, where y and x stand for the image's Cartesian coordinates, or its horizontal and vertical lengths from the origin, and σ (sigma) is the standard deviation of the Gaussian function. Figure 2 shows an appropriate example of an integer-valued convolution kernel with a sigma of 1.0 that approximates a Gaussian.

$$\frac{1}{275}\begin{bmatrix} 1 & 4 & 7 & 4 & 1 \\ 4 & 16 & 26 & 16 & 4 \\ 7 & 26 & 43 & 26 & 7 \\ 4 & 16 & 26 & 16 & 4 \\ 1 & 4 & 7 & 4 & 1 \end{bmatrix}$$

**Figure 2.** A Gaussian smoothing filter's operation

$$G(x,y) = \frac{1}{2\pi\sigma^2} e^{-\frac{x^2+y^2}{2\sigma^2}} \quad (1)$$

Equation (1) represents the Gaussian filter equation. Because Gaussian changes non-linearly between pixels, utilising the mask's centre value to simulate a Gaussian may yield inaccurate results; instead, it integrates the value over the full pixel set, with 275 serving as the mask sum. Afterwards, applying the generated normalised convolutional matrix to the original image portrayed by the matrix, a new set of pixels is formed that includes a weighted average of the neighbouring pixels.

### 3.2.2. Contrast Enhancement

Equation 2 represents the alpha (α) and beta (β) values, which are commonly referred to as the gain and bias parameters, and were used to modify the contrast.

$$g(i,j) = \alpha \times f(i,j) + \beta \quad (2)$$

User-specified beta and alpha values are already implemented by the built-in OpenCV function cv2.convertScaleAbs(). The image's contrast was increased using the global contrast stretching (GCS) technique. Equation 3 states that GCS is performed by dragging an overlapping pane on the lung nodule picture.

$$I_{(a,b)} = \frac{255 \times [I_a(a,b) - x|}{(y-x)} \quad (3)$$

Where, ($I_{(a,b)}$) shows the colour level that will be generated for the image's pixel coordinates (a,b) ( $I_{(a,b)}$), The highest and minimum values for the pixels, y and x, respectively, represent the input colour level.

## 3.3. LNS-DualMAGNet Segmentation

This section first introduces the Dual-path Multi-scale Attention Guided network and then goes over each network component in detail. Among existing networks, DualMAGNet is unique because of its creative architecture that combines attention mechanisms and multi-scale features. This network uses a dual-path design, which allows it to process multiple scales in the data at the same time, in contrast to traditional networks that concentrate on single scales or particular features of the input data. This dual-path structure improves the model's comprehension of both fine-grained details and more general contextual information by making it easier to segment rich, hierarchical features at different levels. Furthermore, by selectively highlighting pertinent features while suppressing noise or less significant elements, the attention mechanisms further enhance the network's learning process and greatly increase its discriminative power. When compared to other single-scale or less adaptive architectures, the DualMAGNet performs better in tasks requiring precise feature localization and nuanced understanding of multi-scale information because of the combination of these elements.

### 3.3.1. Model Architecture

The LNS-DualMAGNet enhances the network's segmentation accuracy by combining an attention mechanism with a multi-scale method. The DualMAF and the MNCA are components of the standard encoder-decoder architecture called the LNS-DualMAGNet. To improve the model's capacity to extract image features, each encoder layer in the LNS-DualMAGNet is merged with a pretrained Resnet 34 model after the DSConv has been utilised as the encoder-decoder portion of the network. Secondly, the purpose of the DualMAF module is to improve the relationship between contextual feature information and to enrich feature details. Ultimately, the MNCA module [27] is proposed by combining the DSConv, atrous convolution, and Normalization-based Attention mechanism in order to achieve more effective multi-scale feature fusion and provide more discriminative feature regions. Algorithm 1 displays the pseudocode for implementing the LNS-DualMAGNet model.

ALGORITHM 1 Function for DualMAGNet Mode

Code:

FUNCTION DualMAGNet(x)

$x$ Relu (BatchNorm (Conv $(x)$))

Encod1 ⟵DSConv1(Pretrained Resnet 34(x))

Encode2 ⟵ DSConv2(Pretrained Resnet34(Encoder1))

Encode3 ⟵ DSConv3(Pretrained Resnet34(Encoder2))

Encode4 ⟵ DSConv4(Pretrained Resnet34(Encoder3))

Decode⟵ $MNCA$(Encoder4)

Decoder 3 ⟵connect (DualMAF(Encoder3, Decoder4),

Decoder4) Decoder 2 ⟵connect(DualMAF(Encoder 2,

DualMAF(Encoder3, Decoder4)), Decoder3)

Decoder1connect(DualMAF(Encoder1,

DualMAF (Encoder2, DualMAF(Encoder 3, Decoder4))), Decoder2) output Sigmoid (Conv(Decoderl))

RETURN output

END FUNCTION

### 3.3.2. Encoder-decoder architecture based on DSConv

Unlike traditional backbone networks, the network under introduction replaces the normal convolutional operation with a DSConv, which serves as the basic building block for both the encoder and the decoder. This adjustment ensures high segmentation performance, allows for an efficient reduction of model parameters, and speeds up training. During the encoder process, smoothly incorporate the pre-trained Resnet34 into the DSConv to improve convergence speed and robustness. Two more modules are increased in the network in order to improve the segmentation of five classes of lung nodule output performance. Firstly, three DualMAF modules are positioned at the skip connection in order to fill in the difference in semantics between the decoder and encoder. Secondly, the rich global feature data is captured by the MNCA module located at the bottom of the encoder. To enhance feature extraction capabilities, the pretrained Resnet34 is further integrated with the DSConv. When the kernel size is $K \times K$, the usual convolution's computational cost is $K \times K \times M \times N \times H \times W$, the computational cost of the DSConv is $K \times K \times M \times H \times W + M \times N \times H \times W$ , as shown in Equation (4).

$$\frac{K \times K \times N \times H \times W + M \times N \times H \times W}{K \times K \times M \times N \times H \times W} = \frac{1}{N} + \frac{1}{k^2} \quad (4)$$

where $M$ is the quantity of channels for input, $N$ is the quantity of channels for output, and $H$ 、$W$ is the height and width of the input feature image. According to equation (4), the DSConv layer replaces the standard convolutional layer in the network, which can reduce the amount of computation by a factor of $1/N + 1/k^2$.

### 3.3.3. Dual-Path Multi-Scale Attention Fusion Module

The paper proposes the DualMAF module as a solution to the intrinsic problems with lung nodule imaging, including the existence of distinct feature information at varying scales and the semantic gap between different layers of feature maps. DualMAF broadens the perceptual area of the network and closes the semantic gap by integrating semantic information from several layers and concentrating on multi-scale features at the same time. Two main parts make up the DualMAF module: channel attention methods and atrous convolution with various expansion rates. Rich feature information can be captured by the atrous convolution method, which can increase the convolution kernel's receptive field without changing the computational parameters [28]. Moreover, channel attention is added to reinforce the interaction between several sequences in order to enhance the feature recognition ability. In conclusion, the DualMAF can enhance feature representation by emphasising location details in shallow branch feature maps and by assisting in deep branch feature maps' gathering of semantic data and global context.

The deep and shallow feature map branches of the DualMAF are divided into separate entities that carry out identical feature processing tasks simultaneously before adding up to produce the ultimate output. Both the shallow and deep branches can be further subdivided into two sub-branches, as shown in Figure 4. The first sub-branch is a multi-receptive field branch that expands the receptive field by means of three atrous convolutions with expansion rates of one, three, and five. The module's objectives are to encode high- and low-level semantic feature maps and extract feature information of various sizes. In the alternative

subbranch, the global contextual feature data is compressed using global average pooling to create an attention vector β, which is subsequently transformed by convolution to further capture the semantic relationships between channels.

The deep layer branch's general structure is identical to that of the shallow layer; however, deconvolution causes it to enlarge in order to aid in the final fusion. Equation (5) provides a description of the DualMAF output.

$$\begin{aligned} \text{out}_S &= [\text{Conv}_{r=1}^{k=3}(x) + \text{Conv}_{r=3}^{k=3}(x) + \text{Conv}_{r=5}^{k=3}(x)] \\ &\quad \otimes \delta_2(\delta_1(\text{Conv}(\text{GAP}(x)))) \\ \text{out}_D &= \text{DeConv}\left[[\text{Conv}_{r=1}^{k=3}(x) + \text{Conv}_{r=3}^{k=3}(x) + \text{Conv}_{r=5}^{k=3}(x)]\right. \\ &\quad \left. \otimes \delta_2(\delta_1(\text{Conv}(\text{GAP}(x))))\right] \\ \text{out} &= \text{out}_S + \text{out}_D \end{aligned} \tag{5}$$

where × refers to the input feature map. $GAP\otimes$ speaks of the worldwide average pooling, and Conv ⊗ refers to $1 \times 1$ convolution. $\delta_1 0$ refers to the ReLU function and $\delta_2$ ⊗ refers to the Sigmoid function, $\text{Conv}_{r=i}^{k=3}(\text{x})$ refers to the atrous convolution ($i = 1,3,5$), the DeConv 0 refers to the deconvolution, out $s$ is the shallow path output, out $t_D$ is the deep path output, and out is the final output.

### 3.3.4. Multi-scale normalized channel attention module

Rich feature information is created in feature maps as network layers go deeper. But within these feature maps, some channels or pixels can be more or less important than others in terms of separating objects from the backdrop or the edges of various structures. As a result, MNCA is suggested as a means of extracting multi-scale characteristics, refining and aggregating multi-scale features, and adaptively learning the significance of each channel. The module can assist the bottom layer in making the most use of data from the global receptive field and more effectively analyse the interdependencies between channels. The MNCA module in Figure 5 is specifically executed in two primary processes.

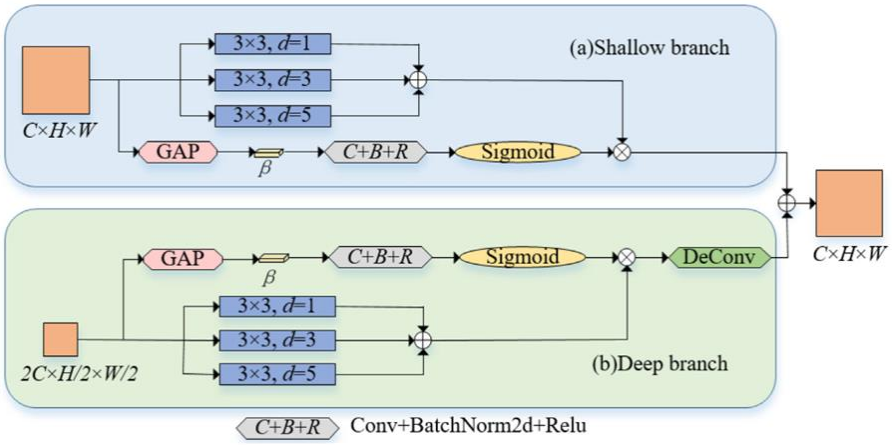


**Figure 3.** DualMAF, Dual-path multi-scale attention fusion architecture

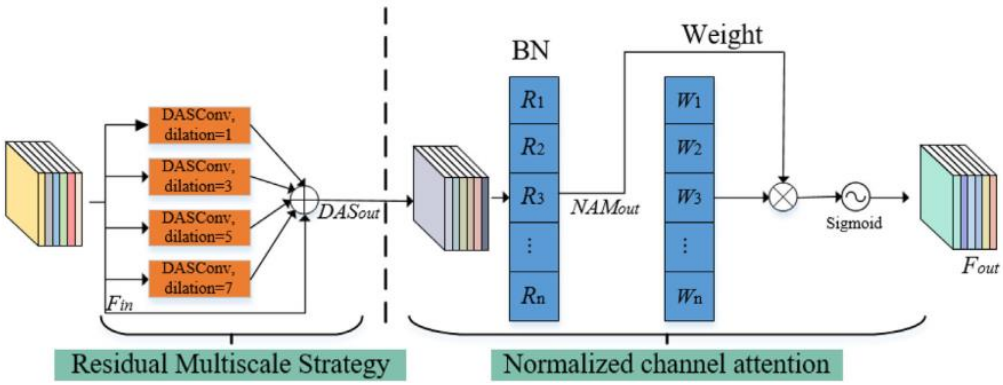


**Figure 4.** MNCA.

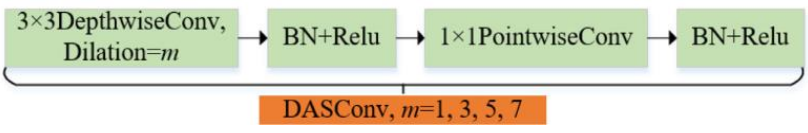


**Figure 5.** DASConv

Depthwise Convolution with a 3x3 Kernel and Dilation=m step entails a depthwise convolution with a dilation factor of 'm'. Spatial filtering is provided by depthwise convolutions, which process each channel independently. Dilation modifies the distance between kernel elements to capture a larger context without appreciably increasing parameters. Batch Normalization (BN) + ReLU technique normalizes the output following depthwise convolution, improving stability and speeding up training. By introducing non-linearity, the Rectified Linear Unit (ReLU) activation function enables the network to learn intricate patterns. Information is combined across channels using a 1x1 convolution (pointwise convolution), which modifies the channel dimensions and permits cross-channel interactions. BN + ReLU: This stage is similar to the previous one in that it refines and normalizes the features even more by applying a second batch normalization and ReLU activation to the pointwise convolution's output. This pattern is used to reduce computational complexity without sacrificing expressive power. Normalization and activation functions are frequently added to this sequence to improve learning and stability.

First, a Depthwise Atrous Separable Convolution (DASConv) module in Figure 6 with expansion ratios of 1, 3, 5, and 7 is suggested as part of the Residual Multi-scale Strategy in order to increase the receptive field for the extraction of rich multi-scale feature information. Furthermore, a residual channel $F_{\text{in}}$ and DASConv are fused, allowing for the extraction of features for objects of different sizes. Equation (6) displays DASConv's output.

$$DAS_{\text{out}} = F_{\text{in}} + \sum_{d=1,3,5,7} D_{ASConv}{}^{d}(F_{\text{in}}) \quad (6)$$

where $DAS_{\text{out}}$ represents the output of the residual multi-scale strategy module, $d$ represents the dilation rate, and DASConv () refers to the DASConv. Second, the normalization-based channel attention is further adopted to strengthen the correlation between feature channels. The $DAS_{\text{out}}$ is batch normalized with the BN function to suppress insignificant weights, so $NAM_{\text{out}}$ contains more significant feature weight information. Then, the channel weights $W_r$ and $NAM_{\text{out}}$ are multiplied to enforce dependencies between feature channels. The process can be expressed in Equation (4)

$$NAM_{\text{out}} = BN(DAS_{\text{out}}) = \gamma \frac{DAS_{\text{out}} - \mu_\beta}{\sqrt{\sigma_\beta^2 + \varepsilon}} + \beta \quad (7)$$

$$W_r = \frac{\lambda_i}{\sum_{j=0} \lambda_j} \quad (8)$$

Based on Equations (6) and (7), the final output of the MNCA module can be expressed by Equation (8).

$$\begin{aligned} F_{\text{out}} &= \text{Sigmoid}\big((W_r)(NAM_{\text{out}})\big) \\ &= \text{Sigmoid}\left(\left(\frac{\lambda_i}{\sum_{j=0} \lambda_j}\right)\left(\gamma \frac{DAS_{\text{out}} - \mu_\beta}{\sqrt{\sigma_\beta^2 + \varepsilon}} + \beta\right)\right) \end{aligned} \quad (9)$$

where $F_{\text{out}}$ is the output feature of the MNCA module according to Equation (9), $r$ is the scale factor of each channel, and $W_r$ refers to the weight of each channel.

### 3.3.5. Loss function

The Dice loss function, which can assess each pixel region separately and then provide feedback to network parameters, is frequently used to calculate regression loss in the lung nodule image segmentation of five classes procedure. In addition, in order to prevent gradient explosion during the proposed network's training phase, this study combines the binary Cross entropy loss function with the dice loss function (BCE). Equation (10) is used in this paper to represent the loss function.

$$\begin{aligned} L_{\text{Dice}} &= 1 - \sum_k^K \frac{2\omega_k \sum_i^N p(k,i) g(k,i)}{\sum_i^N p^2(k,i) + \sum_i^N g^2(k,i)} \\ M &= \sum_i^N g^2(k,i) \log\left(\sum_i^N p^2(k,i)\right) \\ N &= \left(1 - \sum_i^N g^2(k,i)\right) \log\left(1 - \sum_i^N p^2(k,i)\right) \\ L_{Bce} &= -\sum_k^K (M + N) \\ L_{\text{loss}} &= L_{\text{Dice}} + L_{\text{Bce}} \end{aligned} \quad (10)$$

where $N$ is the pixel, $p(k,i) \in [0,1]$ and $g(k,i) \in [0,1]$ represent the prediction probability and the true label respectively, $k$ represents the class, and $L_{Bce}$ represents the BCE Loss function.

## 3.4. Hyperparameter tuning using DBOA

Dugout beetles [29] in the wild roll their excrement into balls and then roll them up as quickly as they can to ward off rival dung beetle rivalry. Such dung beetles are called rolling balls in this paper. The dung beetle will use the light in its surroundings to guide it in the right direction, making the dung ball move in the straightest path feasible. The position of the dung beetle when it moves the dung ball is updated and described by equation (11).

$$\begin{aligned} X_i^{n+1} &= X_i^n + a \cdot b \cdot X_i^{n-1} + B \cdot \Delta x \\ \Delta x &= |X_i^n - X^w| \end{aligned} \quad (11)$$

where $X_i^n$ provides the location data of the dung beetles' $i$-th generation following their $n$-th iteration, where b is an arbitrary number of $[0,0.2]$ it stands for the coefficient of defect. $B$ symbolises a continuous stealing of values from $[1,0]$, and the value of $a$ is assigned -1 or 1, it stands for the different impacts found in nature. It is employed to replicate variations in light intensity and $X^w$ is the worst position in the world.

Furthermore, in low light or on uneven terrain, dung beetles are blind and can't see wherever they are going. They will ascend the dung ball in these circumstances and dance to determine the direction of their next step. The dung beetle uses its dancing to update its position, and its formula is shown in equation (12).

$$X_i^{n+1} = X_i^n + \tan\beta |X_i^n - X_i^{n-1}| \quad 0 \le \beta \le \pi \quad (12)$$

where $|X_i^n - X_i^{n-1}|$ is the separation between the $(n-1)$ −th and $i$-th generations at the n-th and n-th iteration positions?

In order to hide and provide a safe space for their young to grow, In order to reach a safe place, dung beetles instinctively roll their dung balls. Dung beetles must, in the meantime, carefully choose where in a mound of dung balls to lay their eggs. As a result, the following Equation (13) defines the formula for figuring out the spawning limits.

$$LB_1 = \max(X^r \cdot (1-T), LB)$$
$$UB_1 = \min(X^r \cdot (1+T), UB) \quad (13)$$

where $X^r$ is the ideal local location at the moment, and $LB_1$ and $UB_1$ are employed to calculate the spawning area's size, where $LB$ and $UB$ are the optimisation issues' upper and lower bounds. And T=1-n/ $N_{\max}$ where $N_{\max}$ is the highest number of iterations possible.

After the area where dung beetles spawn boundaries have been established, females will only deposit one egg per generation within the area indicated by the aforementioned formula. The female dung beetle can perceive boundary changes in the spawning region and will actively shift her spawning place accordingly. The following equation (14), when applied to dung beetles, determines the optimal places for egg laying.

$$X_i^{n+1} = X^r + B_1 \cdot (X_i^n - LB_1) + B_2 \cdot (X_i^n - UB_1) \quad (14)$$

where $X_i^n$ represents the site of the $i$ -th generation after the $n$ -th iteration, $B_1$ and $B_2$ two arbitrary matrices of $1 \cdot \mathrm{Dim}$ , and the Dim is the algorithm's dimensional size.

Newborn dung beetles are adult dung beetles that emerge from the ground in quest of food. to imitate the natural foraging behaviour of dung beetles, foraging zones were established to direct the insects throughout their foraging activities. Equation (15) is used to determine the foraging boundaries.

$$LB_2 = \max(X^- \cdot (1-T), LB)$$
$$UB_2 = \min(X^- \cdot (1+T), UB) \quad (15)$$

where $X^-$ is the worldwide ideal location, and $LB_2$ and $UB_2$ are employed to establish the upper and lower limits of the dung beetle's food search region. $T$ has the same significance as dung beetles' egg-laying border selection technique.

Equation (16) is listed as the location update formula because the dung beetle will use the borders of its foraging area to calculate its foraging location once its foraging area has been established.

$$X_i^{n+1} = X_i^n + K_1 \cdot (X_i^n - LB_2) + K_2 \cdot (X_i^n - UB_2) \quad (16)$$

where $X_i^n$ is the location of the little dung beetle generation $i$-th at the $n$-th iteration, and $K_1$ is a figure that follows the gaussian distribution, and $K_2$ symbolise a set that is a part of [0,1].

Furthermore, thieving dung beetles are beetle thieves who steal other dung beetles' dung balls from their colonies. Using the preceding equation, it is clear that $X^s$ is the greatest location for dining. Consequently, it is presumed that $X^s$ is the best location for competition. As a result, Equation (17) provides an updated description of where the thieves are located.

$$X_i^{n+1} = X^s + P \cdot f \cdot (|X_i^n - X^r| + |X_i^n - X^-|) \quad (17)$$

where $X_i^n$ is the location of the $i$-th burglar at iteration $t$-th, and $f$ is a stochastic set obeying a normal distribution with size $1 \cdot \mathrm{Dim}$, and $P$ is represented as a constant number.

## 4. Results and Discussion

### 4.1. Experimental Setup

Python is used in the implementation of the suggested LNS-DualMAGNet. The suggested model is trained and tested on an Ubuntu 18.04 desktop running on an Intel Core i5-3470 processor and a Tesla k40c graphics card with 12 G of video memory. During training, the network's parameters are updated for 40 epochs using the DB optimizer, starting with a learning rate of 1 × 10-3 and with a batch size of 4.

In sample output picture 1, the blue zone indicates the presence of a well-circumscribed area; in sample output image 2, the green region indicates the presence of pleural-tail. vascularized area is indicated by the yellow masked region in sample output image 3, juxta-pleural presence is indicated by the red region in sample output image 4, and ground glass opacity is indicated by the dark blue region in sample output image 5, all were scientific image results.

### 4.2. Performance Metrices

To comprehensively and objectively evaluate the segmentation performance of the proposed model, the following metrics are selected: the Area Under receiver operation characteristic Curve (AUC), Hausdorff Distance (HD), Dice Similarity Coefficient (DSC), Accuracy (Acc), Sensitivity (Sen), and Mean IOU (MIOU). Among these, MIOU averages the ratio between the intersection and concatenation between the true labels and the category prediction results to determine how accurate the prediction results were. To gauge how comparable the predicted and ground truth maps are, DSC computes their overlap. The distance between the two groups is calculated using HD, where smaller numbers denote greater resemblance.

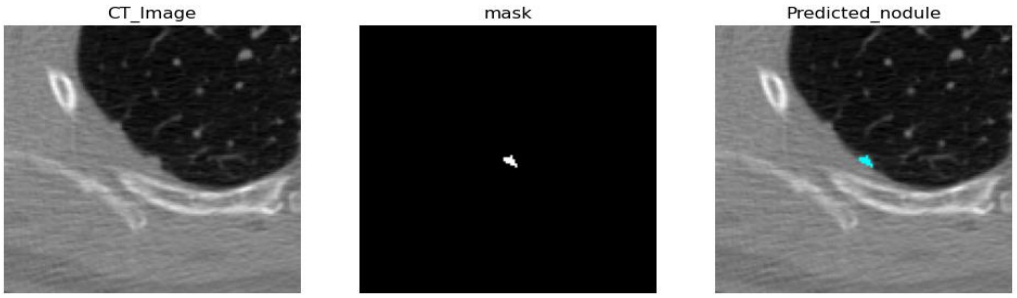


(a) Clearly defined

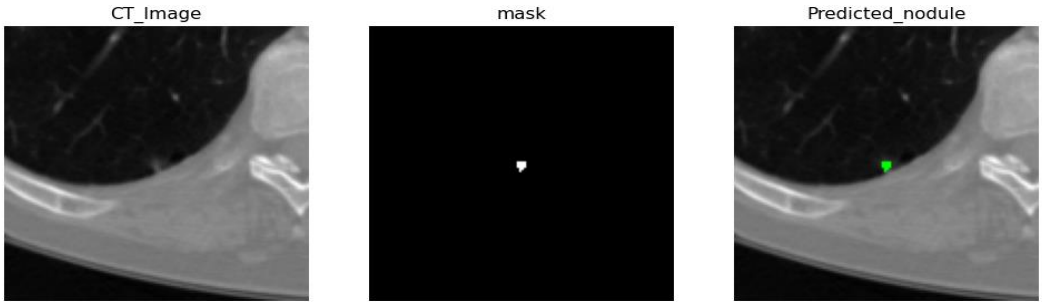


(b) Pneumatic tail


(c) vascularized

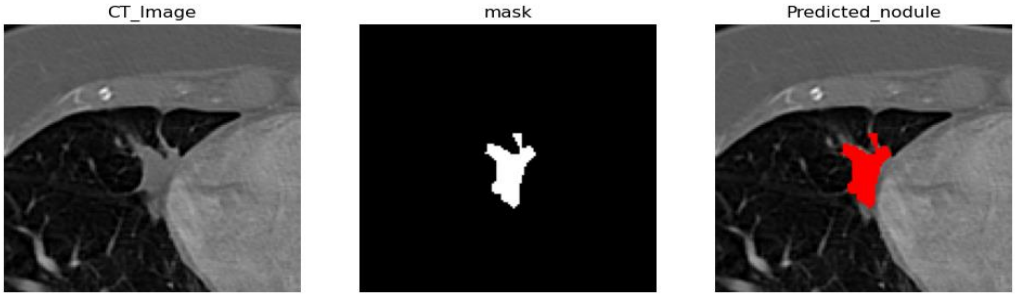


(d) juxta-pleural

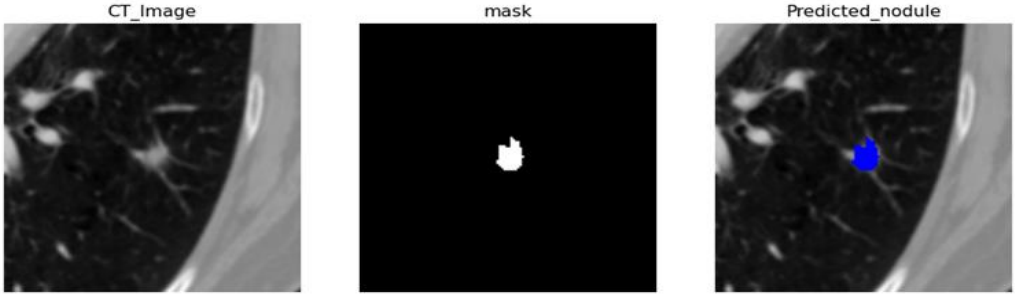


(e) ground glass opacity

**Figure 6.** Segmentation output

ACC measures how many pixels are accurately tagged relative to how many total pixels there are. Better segmentation is indicated by higher accuracy. Sen is the proportion of pixels with properly predicted real labels. AUC also shows the likelihood that the model will accurately predict positive or negative samples; a value nearer 1 denotes superior model performance. Equations provide the specifics (18–23).

$$HD'(S_a, S_b) = \max_{i \in S_a} \min_{j \in S_b} \| i - j \|_2 \quad (18)$$

$$HD(S_a, S_b) = \max\left(HD'(S_a, S_b), HD'(S_b, S_a)\right) \quad (19)$$

where $S_a$ and $S_b$ symbolise the group of target surface locations that the ground truth and CNN, respectively, have segmented.

$$DSC = \frac{2TP}{2TP+FP+FN} \quad (20)$$

$$MIOU = \frac{1}{K+1} \sum_{i=0}^{K} \frac{TP}{TP+FP+FN} \quad (21)$$

$$Acc = \frac{TP+TN}{TP+FP+FN+TN} \quad (22)$$

$$Sen = \frac{TP}{TP+FN} \quad (23)$$

where TP and TN stand for the quantity of pixels that have been appropriately identified as true positives and true negatives, respectively. On the other hand, FP, FN represents the quantity of pixels that are mistakenly identified as false positives and false negatives, respectively.

After taking into consideration the five different classes of lung nodules such as ground glass opacity, juxta-pleural, pleural-tail, vascularized, and well-circumscribed glass—the confusion matrix was created which is shown in Figure 8.

### *Confusion- matrix:*

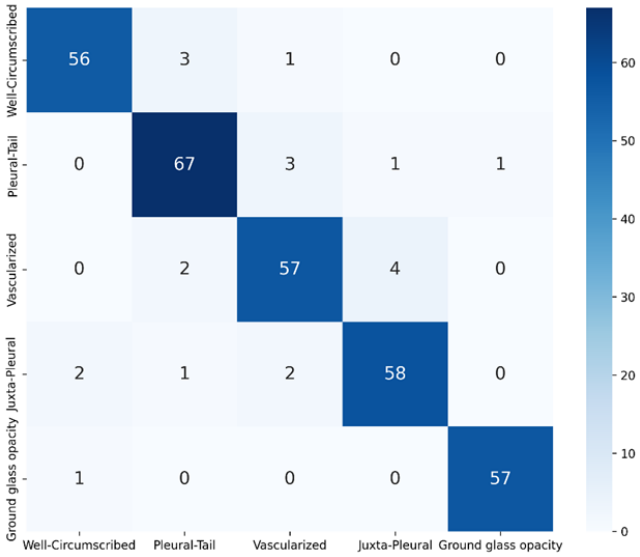


**Figure 7.** Confusion Matrix

### *ROC- curve*

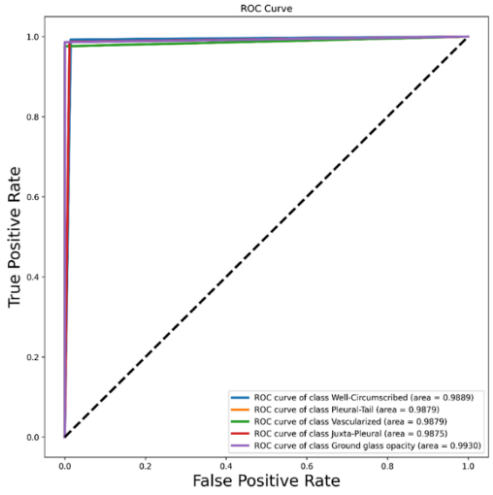


**Figure 8.** ROC curve

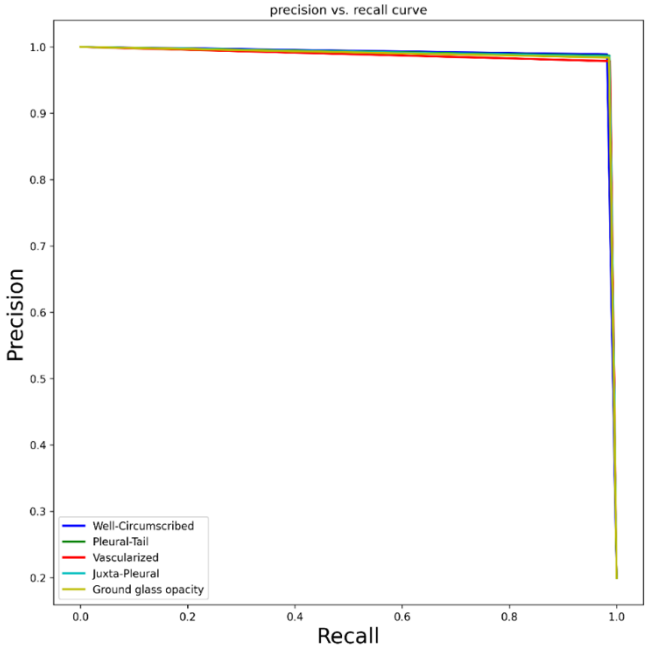


**Figure 9.** Precision vs recall curve

### *Training and Testing Accuracy and Loss*

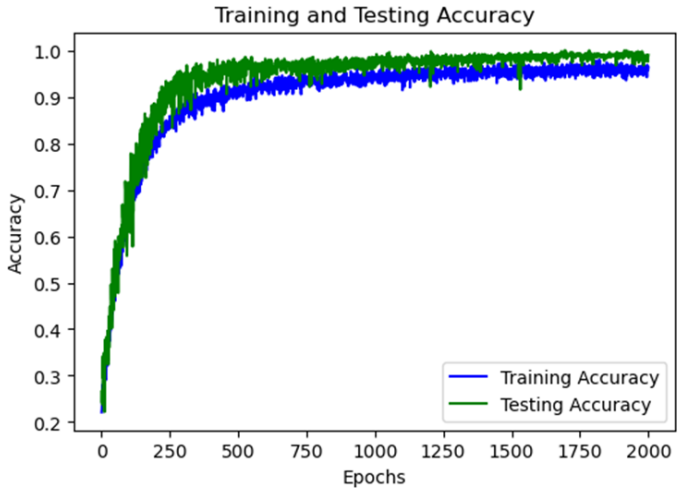


**Figure 10.** Training and testing accuracy illustration

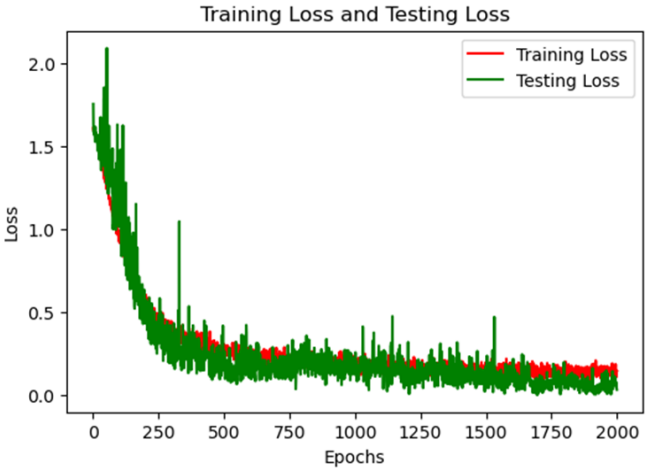


**Figure 11.** Graph of Training and Testing Loss

The ROC curve, which has a true and a false-positive rate, is shown in Figure 9. This is the Precision vs. Recall curve in Figure 10. Accuracy and loss during figures 11 and 12 display the training and testing results.

### 4.3 Comparative Analysis

From table 1 and figure 13 and 14 different approaches to lung nodule segmentation have been developed and tested for effectiveness. Promising results have been observed for DEHA-Net, Bi-FPN, 3DAGNet, Wavelet U-Net++, and LNS-DualMAGNet. Both DEHA-Net and Bi-FPN perform comparably, with Mean Intersection over Union (MIOU) values of 97.07% and Hausdorff Distance (HD) values of 5.61mm and 5.39mm, respectively. Along with remarkable Accuracy (Acc) rates of 99.37% and 99.38%, they both attain high Dice Similarity Coefficient (DSC) scores of 98.33% and 98.35%. They have Area under the Curve (AUC) values of 99% and 99.04%, respectively. With an HD of 5.66mm, 3DAGNet obtains a marginally lower MIOU of 96.95%, but it outperforms in DSC (98.41%), Acc (99.33%), and AUC (99.10%). The Wavelet U-Net++ exhibits commendable segmentation performance, as evidenced by its 96.47% MIOU, 5.63mm HD, 98.14% DSC, 99.34% Acc, and 98.84% AUC. Beyond these, with an HD of 5.42mm, a DSC of 98.71%, an Acc of 99.71%, an outstanding AUC of 99.68%, and an astounding MIOU of 97.32%, LNS-DualMAGNet is clearly superior. The scientific parameters only had taken in comparing the existing and proposed model. These techniques demonstrate improvements in lung nodule segmentation, with LNS-DualMAGNet showing especially encouraging performance on a number of assessment metrics.

From table 2 and figure 15 Key criteria, such as intersection over union (IOU), dice similarity coefficient (DSC), accuracy (Acc), and sensitivity (SE), were used to evaluate a number of segmentation techniques. An IOU of 0.7902, a DSC of 0.7703, an accuracy of 0.9865, and a sensitivity of 0.8487 were all attained by the DC-UNet. Comparable results were shown by the Series atrous convolution augmented U-Net, which had an IOU of 0.7224, a DSC of 0.8110, an accuracy of 0.9870, and a sensitivity of 0.8422. PDD-UNet demonstrated remarkable IOU and DSC values of 0.93 and 0.95, respectively. Its accuracy information was not supplied, and its sensitivity was stated as 0.96. With an IOU of 0.81 and a DSC of 0.88, the Patchwise Iterative Graph Clustering technique performed well, however accuracy and sensitivity data were not available. Lastly, with an IOU of 0.98, a DSC of 0.99, an accuracy of 0.99, and a sensitivity of 0.98, LNS-DualMAGNet demonstrated outstanding performance. Together, these metrics provide information on how well each approach can segment data, with LNS-DualMAGNet demonstrating very strong performance across all assessed parameters.

**Table 1.** Comparison of various methods for segmenting lung nodules on LIDC-IDRI dataset.

| Methods | MIOU (%) | HD (mm) | DSC (%) | Acc (%) | AUC (%) |
|---|---|---|---|---|---|
| DEHA-Net | 97.07 | 5.61 | 98.33 | 99.37 | 99.04 |
| Bi-FPN | 97.07 | 5.39 | 98.35 | 99.38 | 99.00 |
| 3DAGNet | 96.95 | 5.66 | 98.41 | 99.33 | 99.10 |
| Wavelet U-Net++ | 96.47 | 5.63 | 98.14 | 99.34 | 98.84 |
| LNS-DualMAGNet | 97.32 | 5.42 | 98.71 | 99.71 | 99.68 |

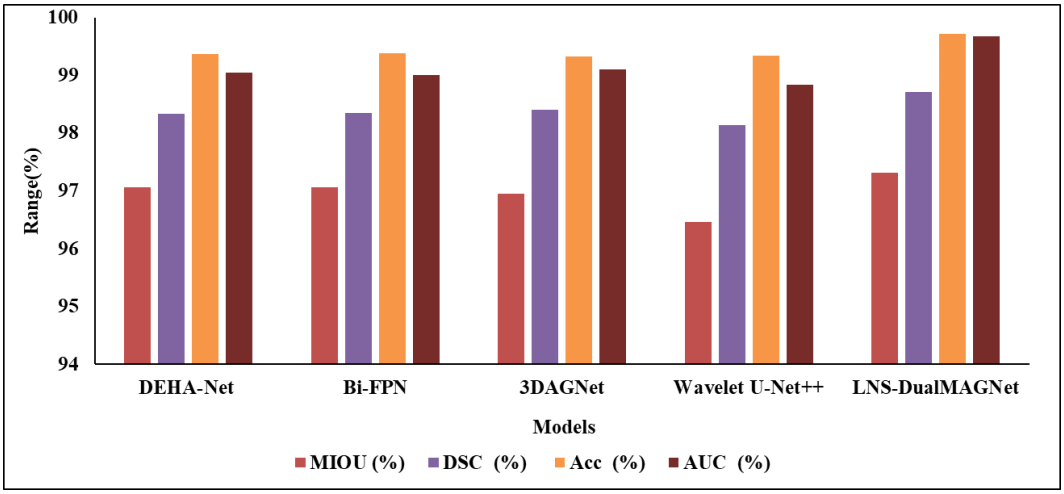


**Figure 12.** Analysis of performance metrics

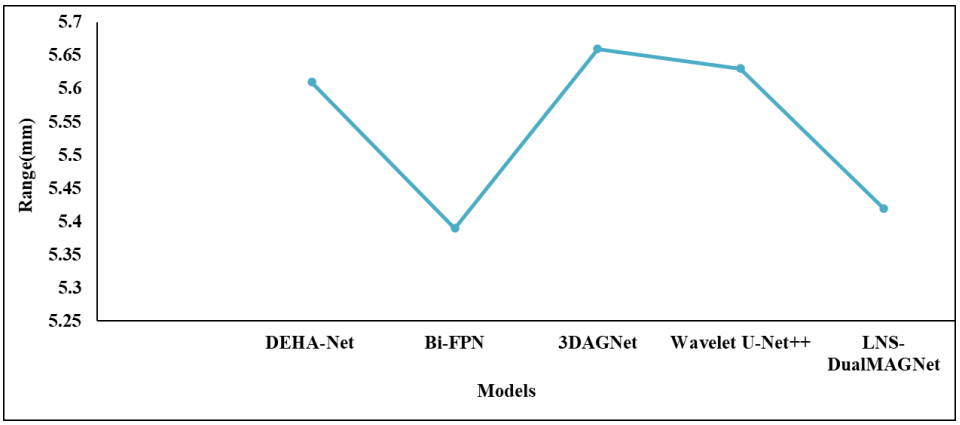


**Figure 13.** HD graphical validation

**Table 2.** Comparing the segmentation of lung nodules using the current techniques

| Methods | IOU | DSC | Acc | SE |
|---|---|---|---|---|
| DC-UNet [14] | 0.7902 | 0.7703 | 0.9865 | 0.8487 |
| Series atrous convolution enhanced U-Net [15] | 0.7224 | 0.8110 | 0.9870 | 0.8422 |
| PDD-UNet [16] | 0.93 | 0.95 | - | 0.96 |
| Patchwise Iterative Graph Clustering [17] | 0.81 | 0.88 | - | - |
| LNS-DualMAGNet | 0.98 | 0.99 | 0.99 | 0.98 |

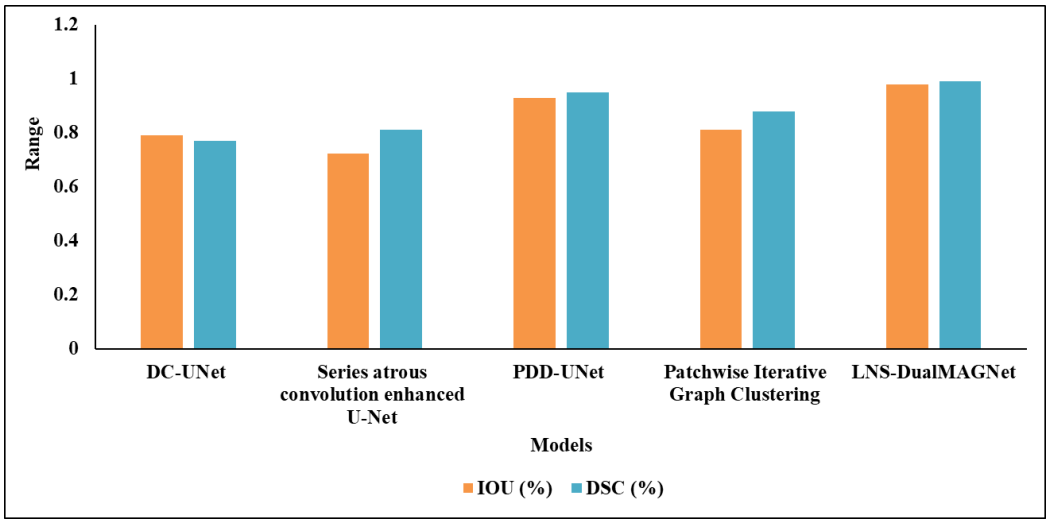


**Figure 14.** Existing models comparison analysis

**Table 3.** Comparison Analysis

| Models | ACC | F1 | JSC | IOU | DSC |
|---|---|---|---|---|---|
| DPAF-Net | 99.0 | 1.0 | 0.99 | 0.94 | 0.97 |
| Random Forest | 0.99 | 0.49 | 0.49 | - | - |
| K-means | 0.99 | 0.49 | 0.49 | 0.0 | 0.0 |
| SVM | 0.99 | 0.49 | 0.49 | 0.0 | 0.0 |

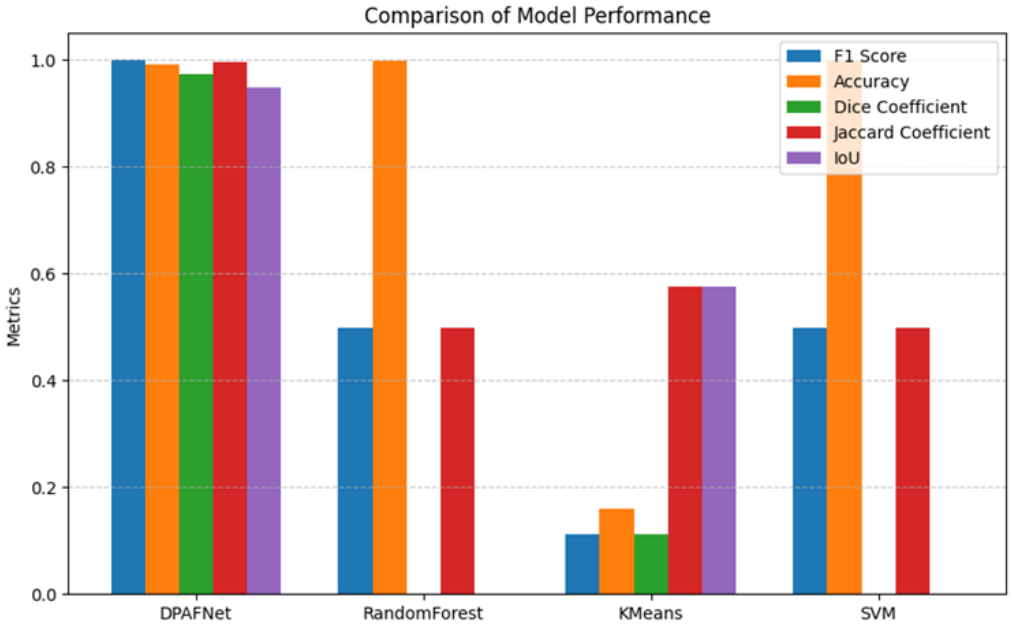


**Figure 15.** Comparison of models performance

From table 3 and figure 16, Several measures including as accuracy (ACC), F1 score (F1), Jaccard similarity coefficient (JSC), intersection over union (IOU), and dice similarity coefficient (DSC), were used to assess the performance of different models. With an accuracy of 99.0%, a flawless F1 score of 1.0, a high Jaccard similarity coefficient of 0.99, an intersection over union of 0.94, and a Dice similarity coefficient of 0.97, the DPAF-Net showed exceptional performance. Conversely, the Random Forest model had a modest F1 score of 0.49, an accuracy of 0.99, and no values for JSC, IOU, or DSC. Comparably, the JSC, IOU, and DSC values of the K-means and SVM models were 0.49, 0.0, and 0.0, respectively, and they also had an accuracy of 0.99 with F1 scores of 0.49. These metrics provide a thorough assessment of the models and demonstrate how well DPAF-Net performs compared to the other models for the long nodule segmentation.

## 5. Conclusion

The study aims to enhance the diagnosis of lung nodules, which are frequently connected to lung cancer, the world's most common cause of cancer-related deaths. The study used preprocessing methods like noise reduction and contrast enhancement on CT scans from the Lung Image Database Consortium and LIDC-IDRI dataset. By enhancing channel interdependence and semantic understanding, the study aimed to improve lung nodule segmentation. Hence, it introduced the LNS-DualMAGNet model, which incorporates novel modules such as the DualMAF and MNCA. The model achieved improved performance by utilizing methods such as Resnet34 block, DSConv and attention mechanisms. By utilizing DBOA to fine-tune the LNS-DualMAGNet hyperparameters, the proposed approach outperformed existing approaches, attaining a 0.99 accuracy and DSC, suggesting that it has the capacity to greatly enhance lung nodule clinical diagnosis.

## References

[1] R.L. Siegel, K.D. Miller, A. Jemal, Cancer statistics, 2020. CA Cancer Journal for Clinicians, 70, (2020) 7–30. https://doi.org/10.3322/caac.21590

[2] WHO. (2020) WHO Report on Cancer: Setting Priorities, Investing Wisely and Providing Care for All. WHO, Geneva, Switzerland.

[3] J. Shao, L. Zhou, S. Y. F Yeung, T. Lei, W. Zhang, X. Yuan, Pulmonary Nodule Detection and Classification Using All-Optical Deep Diffractive Neural Network. Life, 13 (2023)1148. https://doi.org/10.3390/life13051148

[4] M. Usman, Y.G. Shin, DEHA-Net: A Dual-Encoder-Based Hard Attention Network with an Adaptive ROI Mechanism for Lung Nodule Segmentation. Sensors, *23* (2023) 1989. https://doi.org/10.3390/s23041989

[5] Z. Gandhi, P. Gurram, B. Amgai, S.P. Lekkala, A. Lokhandwala, S. Manne, A. Mohammed, H. Koshiya, N. Dewaswala, R. Desai, H. Bhopalwala, S. Ganti, S. Surani, Artificial Intelligence and Lung Cancer: Impact on Improving Patient Outcomes. Cancers, 15 (2023) 5236. https://doi.org/10.3390/cancers15215236

[6] M. Jian, L. Zhang, H. Jin, X. Li, 3DAGNet: 3D Deep Attention and Global Search Network for Pulmonary Nodule Detection. Electronics, 12 (2023) 2333. https://doi.org/10.3390/electronics12102333

[7] W. Wei, S.G. Wang, J.Y. Zhang, X.Y. Togn, B.B. Li, X. Fang, W.R. Pu, Y. Jing Zhou, Y.J. Liu, Implementation of Individualized Low-Dose Computed Tomography-Guided Hook Wire Localization of Pulmonary Nodules: Feasibility and Safety in the Clinical Setting. Diagnostics, 13 (2023) 3235. https://doi.org/10.3390/diagnostics13203235

[8] S.C. Hung, Y.T. Wang, M.H. Tseng, An Interpretable Three-Dimensional Artificial Intelligence Model for Computer-Aided Diagnosis of Lung Nodules in Computed Tomography Images. Cancers, 15 (2023) 4655. https://doi.org/10.3390/cancers15184655

[9] M. Nasir, M.S. Farid, Z. Suhail, & M.H. Khan, Optimal Thresholding for Multi-Window Computed Tomography (CT) to Predict Lung Cancer. Applied Sciences, 13 (2023) 7256. https://doi.org/10.3390/app13127256

[10] K. Cao, H. Tao, Z. Wang, Three-Dimensional Multifaceted Attention Encoder–Decoder Networks for Pulmonary Nodule Detection. Applied Sciences, 13 (2023) 10822. https://doi.org/10.3390/app131910822

[11] Y. Dong, X. Li, Y. Yang, M. Wang, B.A. Gao, Synthesizing Semantic Characteristics Lung Nodules Classification Method Based on 3D Convolutional Neural Network. *Bioengineering*, 10 (2023) 1245. https://doi.org/10.3390/bioengineering10111245

[12] A.A. Alsheikhy, Y. Said, T. Shawly, A.K. Alzahrani, H. Lahza, (2023). A CAD System for Lung Cancer Detection Using Hybrid Deep Learning Techniques. Diagnostics, 13 1174. https://doi.org/10.3390/diagnostics13061174

[13] M. Cellina, L.M. Cacioppa, M. Cè, V. Chiarpenello, M. Costa, Z. Vincenzo, D. Pais, M.V. Bausano, M. Costa, A. Bruno, C. Floridi, (Artificial Intelligence in Lung Cancer Screening: The Future Is Now. Cancers, 15 (2023) 4344. https://doi.org/10.3390/cancers15174344

[14] K.B. Chen, Y. Xuan, A.J. Lin, S.H. Guo, Lung computed tomography image segmentation based on U-Net network fused with dilated convolution. Computer Methods and Programs in Biomedicine, 207 (2021) 106170. https://doi.org/10.1016/j.cmpb.2021.106170

[15] S. Selvadass, P.M. Bruntha, K.M. Sagayam, & H. Gunerhan, (2023) SAtUNet: Series atrous convolution enhanced U-Net for lung nodule segmentation. International Journal of Imaging Systems and Technology. https://doi.org/10.1002/ima.22964

[16] S.A. Agnes, Boundary Aware Semantic Segmentation using Pyramid-dilated Dense U-Net for Lung Segmentation in Computed Tomography Images. Journal of Medical Physics, 48 (2023) 161-174.

[17] S. Modak, E. Abdel-Raheem, L. Rueda, (2023) Lung Nodule Segmentation on CT Scan Images Using Patchwise Iterative Graph Clustering. In 2023 IEEE International Symposium on Circuits and Systems (ISCAS), IEEE, USA. https://doi.org/10.1109/ISCAS46773.2023.10181811

[18] S.A. Agnes, A.A. Solomon, & K. Karthick, Wavelet U-Net++ for accurate lung nodule segmentation in CT scans: Improving early detection and diagnosis of lung cancer. Biomedical Signal Processing and Control, 87 (2024) 105509. https://doi.org/10.1016/j.bspc.2023.105509

[19] Y. Cai, Z. Liu, Y. Zhang, & Z. Yang, MDFN: A Multi-level Dynamic Fusion Network with self-calibrated edge enhancement for lung nodule segmentation. Biomedical Signal Processing and Control, 87 (2024) 105507. https://doi.org/10.1016/j.bspc.2023.105507

[20] D. Bhattacharyya, N. Thirupathi Rao, E.S.N. Joshua, & Y.C. Hu, A bi-directional deep learning architecture for lung nodule semantic segmentation. The Visual Computer, 39(11), (2023) 5245-5261. https://doi.org/10.1007/s00371-022-02657-1

[21] M. Usman, & Y.G. Shin, DEHA-Net: A Dual-Encoder-Based Hard Attention Network with an Adaptive ROI Mechanism for Lung Nodule Segmentation. Sensors, 23 (2023) 1989. https://doi.org/10.3390/s23041989

[22] D. Srivastava, S.K. Srivastava, S.B. Khan, H.R. Singh, S.K. Maakar, A.K. Agarwal, A.A. Malibari, E. Albalawi, Early Detection of Lung Nodules Using a Revolutionized Deep Learning Model. Diagnostics, 13 (2023) 3485. https://doi.org/10.3390/diagnostics13223485

[23] R. Cao, L. Ning, C. Zhou, P. Wei, Y. Ding, D. Tan, & C. Zheng, CFANet: Context Feature Fusion and Attention Mechanism Based Network for Small Target Segmentation in Medical Images. Sensors, 23 (2023) 8739. https://doi.org/10.3390/s23218739

[24] Y. Lyu, & X. Tian, MWG-UNet: Hybrid Deep Learning Framework for Lung Fields and Heart

Segmentation in Chest X-ray Images. Bioengineering, 10 (2023) 1091. https://doi.org/10.3390/bioengineering10091091

[25] S. Basavarajappa, & S. Mahesh, Lung Nodule Segmentation Using Cat Swarm Optimization Based Recurrent Neural Network. International Journal of Intelligent Engineering & Systems, 16 (2023) 458-469. https://doi.org/10.22266/ijies2023.1231.38

[26] A.S. Mubarak, Z.S. Ameen, & F. Al-Turjman, Effect of Gaussian filtered images on Mask RCNN in detection and segmentation of potholes in smart cities. Mathematical Biosciences and Engineering, 20 (2023) 283-295. https://doi.org/10.3934/mbe.2023013

[27] D. Forsström, M. Oscarsson, M. Buhrman, & A. Rozental, A study protocol of a randomized controlled study of internet-based cognitive behavioral therapy for adult attention deficit hyperactivity disorder. Internet Interventions, 33 (2023) 100652. https://doi.org/10.1016/j.invent.2023.100652

[28] B. Wang, H. Yao, D. Song, J. Zhang, & H. Gao, (2023). SSF-Net: A Spatial-Spectral Features Integrated Autoencoder Network for Hyperspectral Unmixing. IEEE Journal of Selected Topics in Applied Earth Observations and Remote Sensing, 1-14. https://doi.org/10.1109/JSTARS.2023.3327549

[29] J. Xue, & B. Shen, Dung beetle optimizer: A new meta-heuristic algorithm for global optimization. The Journal of Supercomputing, 79 (2023) 7305-7336. https://doi.org/10.1007/s11227-022-04959-6

[30] M. Alamgeer, N. Alruwais, H.M. Alshahrani, A. Mohamed, & M. Assiri, Dung Beetle Optimization with Deep Feature Fusion Model for Lung Cancer Detection and Classification. Cancers, 15 (2023) 3982. https://doi.org/10.3390/cancers15153982

## Authors Contribution Statement

K. Sathyamoorthy defined the problem statement, reviewing the literature, manuscript preparation/writing and data collection & analysis part of this research work. Author S. Ravikumar performed the simulation work, paper formatting and proof-reading works. Both authors read and approved the final version of this manuscript.

## Funding:

The authors declare that no funds, grants, or other support were received during the preparation of this manuscript.

## Competing Interests

The authors declare that there are no conflicts of interest regarding the publication of this manuscript.

## Data Availability

Data will be provided upon request.

## Has this article screened for similarity?

Yes

## About the License